ACS OMEGA

Open Access

http://pubs.acs.org/journal/acsodf

Article

Investigations of Water Transport in Shale Reservoir with Dual-Wettability by Using Monte Carlo Method

Tuo Liang,* Weipeng Fan, Bo Yu, Changhua Yang,* and Ming Qu*

Cite This: *ACS Omega* 2023, 8, 48280−48291

Read Online

ACCESS | Metrics & More | Article Recommendations

ABSTRACT: How liquids transport in the shale system has been the focus because of fracturing fluid loss. In this study, a single-nanopore model is established for liquid transport in shale while considering the slip effect and effective viscosity of confined fluids. Then, the fractal Monte Carlo (FMC) model is proposed to upscale the single-pore model into shale porous media. The effects of different transport mechanisms, shale wettability, and pore characteristic parameters on confined liquid flow in shale rock are investigated. Results show that FMC permeabilities are 2−3 orders of magnitude larger than intrinsic and slip-corrected permeabilities in organic matter. However, the slip effect and effective viscosity have little influence on water flow in inorganic matter. With the contact angle of organic pore (θ_{om}) increasing and contact angle of inorganic pore (θ_{in}) decreasing, the effective permeability of the whole shale matrix grows in number. The enhancement factor in the situation of θ_{om} = 170° and θ_{in} = 20° is 4 orders of magnitude larger than the case of θ_{om} = 130° and θ_{in} = 40°, although the close effective macroscopic contact angle (θ_{eff} = 80°) occurs in these two cases, which indicates that shale microscopic wettability has a significant impact on the confined liquid transport. Moreover, with the increase of porosity and maximum pore diameters, shale permeability increases rapidly, but the enhancement factor has the opposite trend. Compared with the tiny impact of the variance of minimum inorganic pore diameters, minimum organic pore diameters have more significant impacts on liquid flow in shale systems, and the enhancement factor also rapidly increases up to 30 times for the case of 0.5 nm because of the strong slip effect.

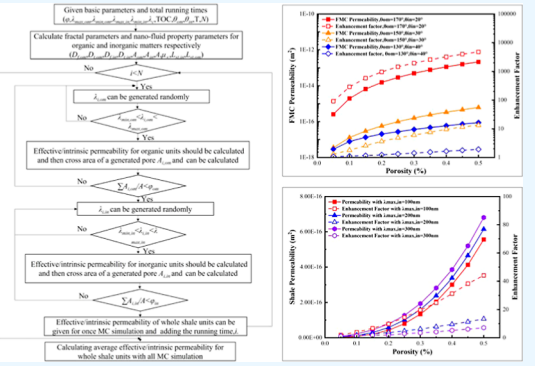

1. INTRODUCTION

With the increase of the world energy demand and decrease of conventional oil/gas resources, unconventional systems, especially shale system, have attracted huge attention all around the world.[1−4] In North America, the commercial development for shale energy named as "Shale Revolution" has successfully ensured its energy requirement and security based on the advanced technology of multistage hydraulic fracturing.[5−7] During the process of this stimulation, more than 2 × 10^4 m^3 of water-slip fracturing fluid is injected into shale formation. However, less than 50% fracturing fluid can only be recovered from the field monitoring data.[8−11] Hence, understanding how water flows in shale matter is critical for fracturing fluid recovery and high-efficiency gas/oil production.

Compared with the conventional oil and gas systems, shale formation has a complex pore space. Xu et al.[12] systematically observed the organic matter pores from Longmaxi Formation by using field emission scanning electron microscopy (FE-SEM). Abundant organic and inorganic pores with nanoscale size have been verified to exist in the shale matrix.[13] Inorganic matter is mainly constituted by clays such as kaolinite, pyrite, Illite, and smectite, all of which present a strong hydrophilic feature. However, organic matter includes kerogen and bitumen with different thermal maturities,[14] both of which vary for highly hydrophobic or mixed-wet matter. Kuila and Prasad[15] made use of N_2 adsorption experiments to report a bimodal pore size distribution for organic and inorganic matter. Complex wettability and nanosize pores lead to a large deviation via applying the classic Hagen−Poiseuille (HP) equation to describe the liquid flow in shale nanopores. Based on molecular dynamic (MD) simulations, Hu et al.[16] established an activated organic kerogen model to reveal the behaviors of water and octane in nanopores. Results indicate that the distribution of water and octane is related to pore morphology, surface activation, and pore size. Zhan et al.[17] used MD simulation to investigate water transport in inorganic slit-like nanopores. In their studies, slip effect and effective viscosity near the wall play a critical role in the confined water flow, and up to 50% underestimation of

Received: October 1, 2023
Revised: November 19, 2023
Accepted: November 21, 2023
Published: December 5, 2023

Table 1. Brief Description of Each Model with Its Limitations

ref	description	model limitation
Hu et al.[16]	an activated organic kerogen model to reveal the behaviors of water and octane in nanopores by MD simulation	single-nanopore model, small-scale simulation, and large cost computation
Zhan et al.[17]	water transport in inorganic slit-like nanopores by MD simulation	
Zhao et al.[18] and Wang et al.[19]	a nanoscale lattice Boltzmann model (LBM) to study water transport in a single-pore and nanoporous media	small-scale simulation and large cost computation
Afsharpoor and Javadpour[20]	coupled computational fluid dynamics (CFD) with the pore network model (PNM) to upscale water transport from a single-nanopore to porous media	small-scale simulation and large cost computation
Wu et al.[21]	a simple analytical single-pore model to show confined water flow with the relationship between confined effect and pore dimension via fitting the results of MD and experiments	Single-nanopore model, not considering the heterogeneity of organic and inorganic matter
Sun et al.[22]	a single-pore model was also set up for confined water flow based on a hierarchical model	Single-nanopore model, not considering the heterogeneity of organic and inorganic matter
Wang and Cheng[33]	coupled fractal theory with two-fluid model to investigate water flow in shale porous media	only considering the true slip length, not considering the heterogeneity of organic and inorganic matter
Zhang et al.[34] and Zeng et al.[36]	a semianalytical fractal model to investigate water flow in shale porous media	large cost computation

volumetric flux will happen as the no-slip HP equation is applied. Zhao et al.[18] set up a nanoscale lattice Boltzmann model (LBM) to study water transport in single-pore and nanoporous media. Meanwhile, nanoscale effects including slip length and effective viscosity were considered in their model. Furthermore, Wang et al.[19] introduced the varying interfacial water viscosity into the boundary conditions of LBM simulation, which matched well with the theoretical formula at different pore sizes. Afsharpoor and Javadpour[20] coupled computational fluid dynamics (CFD) with the pore network model (PNM) to upscale water transport from a single-nanopore to porous media. Although microscale and mesoscopic simulations such as MD, LBM, and CFD-PNM are accurate methods to describe the water flow in nanopores, huge computational consumption leads to the restriction for macroscale numerical simulation and production field application. Wu et al.[21] obtained the relationship between confined effect (effective viscosity and slip length of confined water with different contact angles) and pore dimension via fitting the results of MD and experiments. By the application of these research achievements, a simple analytical single-pore model was established to show confined water flow. Results demonstrate that the flow capacity of confined water can be up to 10^7 times that of the given results of no-slip HP equation. Sun et al.[22] divided the distribution of confined water in nanopores into two parts: interfacial region and bulk region. Lan et al.[23] investigated the wetting behaviors of rock samples by conducting spontaneous imbibition experiments with oil and water and discussed the correlation between pore connectivity, contact angle, and wettability. Arif et al.[24] reviewed the recently published data sets on shale contact angle measurements. Zhao et al.[25] established a single-nanopore model by considering mixed wettability, surface roughness, varying viscosity, and the effects triggered by adsorbed organic matter. In this work, a single-pore model was also set up for confined water flow based on a hierarchical model with diffident fluid properties and slip-corrected boundary. In summary, the single-nanopore model considering the confinement effect is simple to apply for microscopical simulations, but as for a complex porous media of shale matrix, the single-nanopore model should be upscaled to describe the water flow in shale porous media.

Fractal theory has been verified to be a strong tool to achieve the single-pore model into a porous media model.[26−29] Several researchers[30−32] have reported that shale matrix is a kind of fractal porous media and its pore size distribution (PSD) satisfies self-similar fractal scaling law. Wang and Cheng[33] coupled the fractal theory with the two-fluid model to investigate the water flow in shale porous media. In their paper, an analytical permeability model was derived by considering only the true slip length. Zhang et al.[34] derived a semianalytical fractal model to investigate the water flow in shale porous media via considering the weighted average viscosity of the interface and bulk region. In order to represent the distribution of organic patch, the statistical model proposed by Naraghi and Javadpour[35] was applied to obtain the permeability of whole shale matrix. Zeng et al.[36] comprehensively considered the relationship among the pore size, effective slip length, and confined viscosity into their model, and they made effort to verify a fact that the confined effect cannot be ignored for liquid transport in shale matter. However, for the above concise models, numerical methods must be applied to solve these nonlinear models, which leads to a huge computational cost. Monte Carlo (MC) simulation coupled with the fractal theory has been widely applied to nonlinear models due to the advantages of good convergence and small storage. Yu et al.[37] applied MC simulation to obtain the permeability of bidispersed fractal porous media. In addition, fractal Monte Carlo method (FMC) has also been used in shale gas flow,[38] two-phase flow,[39−41] fractured porous media,[42,43] and other fields.[44−46] The different models with their limitations proposed by previous researchers are summarized in Table 1. Nevertheless, it has not been reported that the FMC method is applied to simulate liquid transport in shale formation while considering the effective slip effect and varying viscosity of the confined fluid, which will be the focused point of our study.

In this paper, a single-nanopore model was first established while considering the slip effect and effective viscosity of the confined fluid. Then, fractal theory was introduced to upscale the single-pore model into a porous model, and the corresponding flow flux model of confined water was derived. Besides, the FMC model was proposed to calculate the permeability of shale matter and enhancement factor. Meanwhile, a detailed algorithm was given for the FMC simulation process, and the verified case of FMC was implemented. Finally, the influence of different transport mechanisms, shale wettability, and pore characteristic parameters on the confined liquid flow in shale matter was discussed.

https://doi.org/10.1021/acsomega.3c07609
ACS Omega 2023, 8, 48280−48291

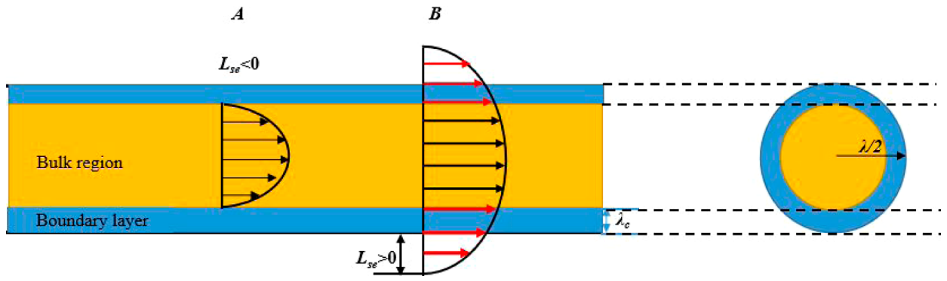

Figure 1. Combined liquid transport in a single shale nanotube for two situations: case A (L_{se} < 0 for inorganic pore because of multilayer sticking effect[21]) and case B (L_{se} > 0 for organic pore because of strong slip effect).

2. MATHEMATICAL MODEL DEVELOPMENT

2.1. Liquid Transport in a Single-Capillary Nanotube.

Shale systems include organic and inorganic components, and there are abundant nanopores in organic and inorganic matter. Many research works have been done to show that the no-slip Hagen−Poiseuille (HP) equation is not suitable to describe the liquid flow in confined nanopores.[47−49] In addition to strong interactions between water and pore walls, the fluid viscosity near the wall deviates from that of bulk water. In this section, the slip boundary and effective viscosity of confined fluid are adopted into the HP equation to present the liquid transport in shale nanotubes, as shown in Figure 1.

Considering the slip boundary and effective viscosity, liquid flow in capillary nanotubes can be described by the corrected Navier−Stokes equation, as in eq 1

$$\begin{cases} \dfrac{\mu_d}{r}\dfrac{d}{dr}\left(r\dfrac{du}{dr}\right) = \dfrac{dp}{dx} \\ \left.\dfrac{du}{dr}\right|_{r=0} = 0 \\ u|_{r=\lambda/2} = -L_{se}\left.\dfrac{du}{dr}\right|_{r=\lambda/2} \end{cases} \tag{1}$$

where u is the fluid flow velocity, m/s; p is the fluid pressure, Pa; r is the pore radius, m; λ is the pore diameter, m; μ_d is the effective viscosity of the confined fluid, Ps·s; and L_{se} is the effective slip length, m, which will be introduced in the next part.

2.1.1. Effective Viscosity of Confined Fluid. In order to describe the effective viscosity of the confined fluid, Wu et al.[21] put forward the weighted average of viscosities in the bulk region and near-wall region as eq 2

$$\mu_d = \mu_i\frac{A_i}{A_t} + \mu_\infty\left(1 - \frac{A_i}{A_t}\right) \tag{2}$$

where μ_i is the effective viscosity of the interface region, Ps·s; A_t is the total cross-section area of a single nanotube, m^2; A_i is the cross-section area of the interface region, m^2, and it can be adopted by eq 3; μ_∞ is the viscosity of the bulk fluid, Ps·s, and it can be adopted by eq 4.[50]

$$A_i = \pi[(\lambda/2)^2 - (\lambda/2 - \lambda_c)^2] \tag{3}$$

$$\mu_\infty = \frac{(T - 273.15) + 246}{[0.05594(T - 273.15) + 5.2842](T - 273.15) + 137.37} \tag{4}$$

where λ_c is the critical thickness, and it has been determined to be 0.7 nm by experiments and MD simulations.[51,52] T is the system temperature, K, and it is worth to note that the bulk fluid viscosity in eq 4 is correct when the temperature can vary between 273.15 and 423.15 K.

Despite the bulk fluid viscosity, the viscosity in the interface region can be strongly affected by the interaction from the pore walls. A fitted relationship between wettability and the ratio of viscosities in different regions can be given as eq 5[21]

$$\frac{\mu_i}{\mu_\infty} = -0.018\theta + 3.25 \tag{5}$$

where θ is the contact angle, °.

2.1.2. Effective Slip Length. True slip length depends on the strength of water−wall interaction, and it can be determined by surface wettability. Wu et al.[21] presented a fitting formula to bridge the contact angle and true slip length as eq 6

$$L_{st} = \frac{C}{(1 + \cos\theta)^2} \tag{6}$$

where L_{st} is the true slip length, m; and C is the fitted coefficient, which is equal to 0.41 by molecular dynamics simulation.

Slip phenomenon of the confined fluid is not only affected by surface wettability but also confined water viscosity and pore size, and the effective slip length can be calculated by two parts, which can be divided into true slip and apparent slip as eq 7.

$$L_{se} = L_{sa} + L_{st} = \left[\frac{\mu_\infty}{\mu_d} - 1\right]\left(\frac{\lambda}{8} + L_{st}\right) + L_{st} \tag{7}$$

where L_{se} is the effective slip length, m; and L_{sa} is the apparent slip length, m. Both effective viscosity and effective slip length are the functions of pore size, which result in the strong nonlinearity for the analytical fractal model. Hence, it is suitable to make use of the fractal Monte Carlo model to simulate the nonlinear flow for the confined fluid.

The flow velocity of the confined fluid is given as eq 8 by solving eq 1 as

$$u = \frac{1}{4\mu_d}\frac{dp}{dx}\left(\frac{\lambda^2}{4} + \lambda L_{se} - r^2\right) \tag{8}$$

By the integration of eq 8, the fluid flux in a single-capillary nanotube can be adopted as eq 9

https://doi.org/10.1021/acsomega.3c07609
ACS Omega 2023, 8, 48280−48291

$$q = \int_0^{\lambda/2} \frac{1}{4\mu_d}\frac{dp}{dx}\left(\frac{\lambda^2}{4} + \lambda L_{se} - r^2\right)2\pi r\, dr = G\frac{\lambda^4}{\mu_d}\frac{dp}{dx}\left(1 + \frac{8L_{se}}{\lambda}\right) \quad (9)$$

where q is the fluid flux, m^3/s; and G is the shape factor ($\pi/128$ for the circular pore).

2.2. Liquid Transport in Fractal Porous Media. Pore size distribution of the shale system has been verified to obey the fractal geometry. Based on the fractal scaling law, Yu[53] proposed the cumulative size distribution of pores in porous media as eq 10

$$N(L \geq \lambda) = \left(\frac{\lambda_{max}}{\lambda}\right)^{D_f} \quad (10)$$

where N is the pore number; L is the length scale, m; λ_{max} is the maximum pore diameter of porous media, m; and D_f is the pore fractal dimension. Differentiating the above equation, the total number of pores between λ and $\lambda + d\lambda$ can be obtained as eq 11

$$-dN = D_f \lambda_{max}^{D_f} \lambda^{-(D_f+1)}\, d\lambda \quad (11)$$

Dividing eqs 10 by 11 can generate the following eq 12

$$-\frac{dN}{N} = D_f \lambda_{min}^{D_f} \lambda^{-(D_f+1)}\, d\lambda = f(\lambda)\, d\lambda \quad (12)$$

where $f(\lambda) = D_f \lambda_{min}^{D_f} \lambda^{-(D_f+1)}$ is the probability density function of pore distribution.[53]

Considering the tortuosity of a single pore, the relationship between the total length and pore diameter can be given as eq 13 with fractal theory[53]

$$L = L_0^{D_T} \lambda^{(1-D_T)} \quad (13)$$

where L_0 is the representative length of straight capillary, m; D_T is the tortuosity fractal dimension, and a higher value of D_T corresponds to a higher tortuosity of pores.

In order to determine the fractal parameters, the box-counting method with image processing or the theoretical method is usually used to determine the values.[54] In this paper, the theoretical method is adopted as eq 14

$$D_f = d_E - \frac{\ln\phi}{\ln(\lambda_{min}/\lambda_{max})} \quad (14)$$

where d_E is the Euclidean dimension, and d_E is equal to 2 for 2D space or 3 for 3D space, respectively; ϕ is the porosity of the porous media.

The tortuosity fractal dimension D_T is expressed as[53] eq 15

$$D_T = 1 + \frac{\ln \tau_{av}}{\ln(L_0/\lambda_{av})} \quad (15)$$

where τ_{av} is the average tortuosity of pores, and λ_{av} is the average pore diameter of the rock core, both of which can be given as[53] eqs 16 and 17

$$\tau_{av} = 0.5\left[1 + 0.5\sqrt{1-\phi} + \sqrt{1-\phi}\,\frac{\sqrt{(1/\sqrt{1-\phi} - 1)^2 + 0.25}}{1 - \sqrt{1-\phi}}\right] \quad (16)$$

$$\lambda_{av} = \frac{D_f}{D_f - 1}\lambda_{min}\left[1 - \left(\frac{\lambda_{min}}{\lambda_{max}}\right)^{D_f - 1}\right] \quad (17)$$

According to the definition of the capillary model, the total cross-sectional area of porous media is calculated as eq 18

$$A = \frac{\int_{\lambda_{min}}^{\lambda_{max}} \pi\lambda^2(-dN)}{4\phi} = \frac{\pi D_f \lambda_{max}^2}{4\phi(2 - D_f)}\left[1 - \left(\frac{\lambda_{min}}{\lambda_{max}}\right)^{2-D_f}\right] \quad (18)$$

where A is the total cross-sectional area of the porous media, m^2.

Shale system has abundant organic and inorganic pores, and the pore size of organic pore is usually smaller than that of inorganic pore by 1−2 orders of magnitude based on nitrogen adsorption test[15] or FIB-SEM images.[55] Besides, the interface feature of the organic pore is different from that of the inorganic pore; therefore, it is necessary to distinguish the modeling process in organic and inorganic matter.

Considering eq 9, the liquid flow rate in a single organic pore can be given as eq 19

$$q_{om} = G\frac{\lambda_{om}^4}{\mu_{dom}}\frac{dp}{dx}\left(1 + \frac{8L_{seom}}{\lambda_{om}}\right) \quad (19)$$

where q_{om} is the liquid flow rate in a single organic pore, m^3/s; λ_{om} is the pore diameter of organic pore, m; μ_{dom} is the effective viscosity of organic matter, Ps·s; and L_{seom} is the effective slip length of organic pore, m.

The total flow rate for organic matter can be calculated as eq 20

$$Q_{om} = \sum_{i=1}^{n} q_{om} = \sum_{i=1}^{n} G\frac{\lambda_{i,om}^4}{\mu_{i,dom}}\frac{dp}{dx}\left(1 + \frac{8L_{i,seom}}{\lambda_{i,om}}\right) \quad (20)$$

where n is the total number of organic pores. With a similar process, the total flow rate for inorganic matter is given as eq 21

$$Q_{in} = \sum_{i=1}^{m} q_{in} = \sum_{i=1}^{m} G\frac{\lambda_{i,in}^4}{\mu_{i,din}}\frac{dp}{dx}\left(1 + \frac{8L_{i,sein}}{\lambda_{i,in}}\right) \quad (21)$$

where q_{in} is the flow rate in a single inorganic pore, m^3/s; m is the total number of inorganic pores; λ_{in} is the pore diameter of inorganic pore, m; μ_{din} is the effective viscosity of inorganic matter, Ps·s; and L_{sein} is the effective slip length of inorganic pore, m.

The total flow rate for a shale system is the summation of that in organic and inorganic matter, as seen in eq 22.

https://doi.org/10.1021/acsomega.3c07609
ACS Omega 2023, 8, 48280−48291

$$Q = Q_{om} + Q_{in} = \sum_{i=1}^{n} G\frac{\lambda_{i,om}^{4}}{\mu_{i,dom}}\frac{dp}{dx}\left(1 + \frac{8L_{i,seom}}{\lambda_{i,om}}\right) + \sum_{i=1}^{m} G\frac{\lambda_{i,in}^{4}}{\mu_{i,din}}\frac{dp}{dx}\left(1 + \frac{8L_{i,sein}}{\lambda_{i,in}}\right) \quad (22)$$

Substituting eq 13 into eq 22, the total flow rate for the shale system can be adopted as eq 23

$$Q = GL_0^{1-D_{Tom}}\frac{\Delta p}{L_0}\sum_{i=1}^{n}\frac{\lambda_{i,om}^{3+D_{Tom}}}{\mu_{i,dom}}\left(1 + \frac{8L_{i,seom}}{\lambda_{i,om}}\right) + GL_0^{1-D_{Tin}}\frac{\Delta p}{L_0}\sum_{i=1}^{m}\frac{\lambda_{i,in}^{3+D_{Tin}}}{\mu_{i,din}}\left(1 + \frac{8L_{i,sein}}{\lambda_{i,in}}\right) \quad (23)$$

where D_{Tom} and D_{Tin} are the tortuosity fractal dimensions for organic and inorganic matters, separately.

According to the classic Darcy's law, the total flow rate for a shale system can be also written as eq 24

$$Q = \frac{K_e}{\mu_\infty}A\frac{\Delta p}{L_0} \quad (24)$$

where K_e is the effective permeability for the shale system, m^2. In addition, the relationship between A and L_0 can be given by eq 25.[37]

$$L_0 = \sqrt{A} \quad (25)$$

Comparing eq 23 with eq 24, the effective permeability for the shale system can be presented as eq 26

$$K_e = K_{e,om} = K_{e,in} = GA^{-(1+D_{Tom})/2}\sum_{i=1}^{n}\frac{\lambda_{i,om}^{3+D_{Tom}}}{\mu_{i,dom}}\left(1 + \frac{8L_{i,seom}}{\lambda_{i,om}}\right) + GA^{-(1+D_{Tin})/2}\sum_{i=1}^{m}\frac{\lambda_{i,in}^{3+D_{Tin}}}{\mu_{i,din}}\left(1 + \frac{8L_{i,sein}}{\lambda_{i,in}}\right) \quad (26)$$

When the slip effect is ignored, the intrinsic permeability for the shale system can be given as eq 27

$$K_\infty = K_{\infty,om} + K_{\infty,in} = GA^{-(1+D_{Tom})/2}\sum_{i=1}^{n}\frac{\lambda_{i,om}^{3+D_{Tom}}}{\mu_{i,dom}} + GA^{-(1+D_{Tin})/2}\sum_{i=1}^{m}\frac{\lambda_{i,in}^{3+D_{Tin}}}{\mu_{i,din}} \quad (27)$$

where K_∞ is the intrinsic permeability for shale system, m^2. From eq 26 and 27, the shale permeability is the summation of two parts: organic matter permeability and inorganic matter permeability.

The enhancement factor (ε) defined by the ratio of flow rate with slip effect and that using a bulk viscosity and no-slip boundary can be proposed to represent the influence of the slip effect, as seen in eq 28.

$$\varepsilon = \frac{Q}{Q_\infty} = \frac{K_e}{K_\infty} = \left[A^{-(1+D_{Tom})/2}\sum_{i=1}^{n}\frac{\lambda_{i,om}^{3+D_{Tom}}}{\mu_{i,dom}}\left(1 + \frac{8L_{i,seom}}{\lambda_{i,om}}\right) + A^{-(1+D_{Tin})/2}\sum_{i=1}^{m}\frac{\lambda_{i,in}^{3+D_{Tin}}}{\mu_{i,din}}\left(1 + \frac{8L_{i,sein}}{\lambda_{i,in}}\right)\right] \Big/ \left[A^{-(1+D_{Tom})/2}\sum_{i=1}^{n}\frac{\lambda_{i,om}^{3+D_{Tom}}}{\mu_{i,dom}} + A^{-(1+D_{Tin})/2}\sum_{i=1}^{m}\frac{\lambda_{i,in}^{3+D_{Tin}}}{\mu_{i,din}}\right] \quad (28)$$

From eqs 26 and 28, the effective permeability and enhancement factor are observed to be related by pore geometry size, effective slip length, and effective viscosity, all of which are the functions of pore size. Based on the fractal Monte Carlo theory,[37] the ith pore diameter for organic and inorganic matter can be obtained as eqs 29 and 30

$$\lambda_{i,om} = \frac{\lambda_{om,min}}{(1 - R_i)^{1/D_{fom}}} \quad (29)$$

$$\lambda_{i,in} = \frac{\lambda_{in,min}}{(1 - R_i)^{1/D_{fin}}} \quad (30)$$

where $\lambda_{om,min}$ and $\lambda_{in,min}$ are the minimum pore diameters of organic and inorganic matter, respectively, m; D_{fom} and D_{fin} are the pore fractal dimensions of organic and inorganic matter, respectively; and R_i is the random number from 0 to 1 and can be produced by Monte Carlo simulations.

In order to carry out the fractal Monte Carlo simulation for liquid effective permeability of the shale system, the detailed flowchart is shown as Figure 2, and the specific algorithm is explained as follows.

Step 1. The basic parameters are input from experiments or image processing, including shale porosity, maximum pore diameter, minimum pore diameter for organic and inorganic matter, critical thickness, and system temperature. The contact angles for inorganic and organic matter are given from 0 to 90° or 90 to 180°, respectively. It is noted that the organic matter content (TOC, the ratio of total area of organic pores to all shale pore area) is usually defined to represent the amount of organic matter in the shale system.[56]

Step 2. The critical parameters should be determined. Applying eqs 14 and 15, the pore fractal dimension and tortuosity fractal dimension are calculated for organic and inorganic matter, both of which should be made use of own parameters. In addition, the bulk viscosity should be calculated by eq 4.

Step 3. One random number for the organic pore diameter should be generated with eq 29, and it should be checked if its value varies between the minimum organic pore diameter and maximum organic pore diameter.

Step 4. The cross-section area of organic matter A_{om} is calculated, and if A_{om}/A is less than organic porosity ϕ_{on}($\phi_{on} = \phi \times$ TOC), the effective/intrinsic permeability for organic units should be calculated by eqs 26 and 27, otherwise go to next step.

Step 5. With a similar process from Step 3 to 4, the effective/intrinsic permeability for inorganic units can be calculated based on inorganic matter parameters.

Step 6. Summing the results of Steps 4 and 5, the effective/intrinsic permeability of whole shale units can be given with one MC simulation.

Step 7. In order to remove the uncertainty of MC simulation, Steps 3 to 6 are repeated to calculate the average

https://doi.org/10.1021/acsomega.3c07609
ACS Omega 2023, 8, 48280−48291

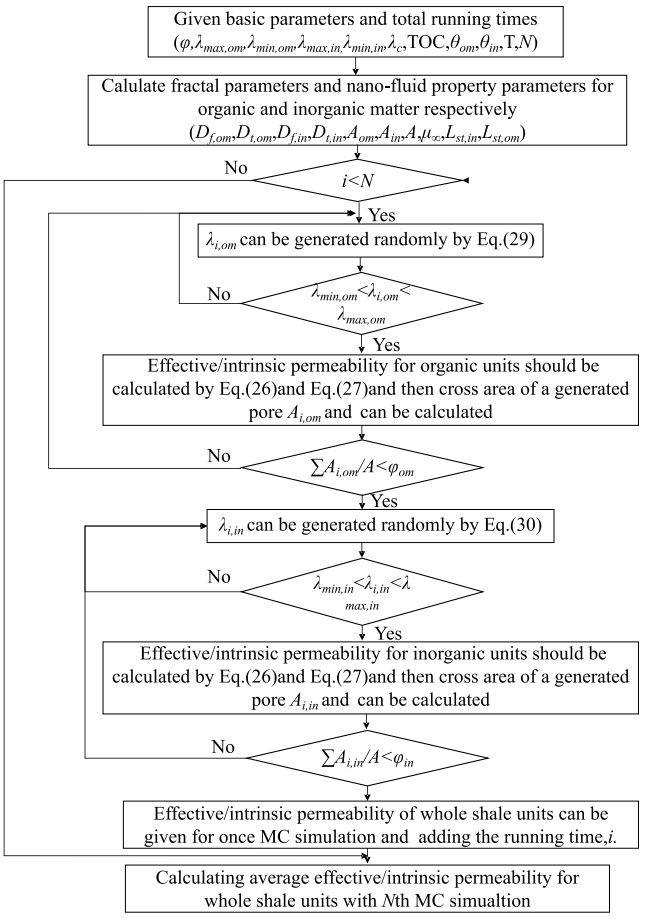

Figure 2. Flowchart for FMC simulation of liquid transport in shale matter.

effective/intrinsic permeability for whole shale units for the given run times.

For the model proposed in this article, three applicable conditions should be focused. First of all, circular shale pores are used in our paper to derive the FMC model; thus, other pore shapes such as square pore, rectangle pore, and slit pore should be treated for FMC simulations.[20,57] Second, bulk fluid viscosity in eq 4 is correct when the temperature can vary between 273.15 and 423.15 K.[50] Hence, if the formation temperature of shale reservoirs goes beyond the scope, a new viscosity model should be set up in the future. Finally, microfractures usually exist in shale formation,[58] which is not considered in our model and should be discussed in the future.

3. MODEL VALIDATION

In order to verify the FMC model, the analytical permeability model, shown in eq 31, is derived only considering the true slip and bulk viscosity. From eq 31, the analytical intrinsic permeability model can be also obtained while ignoring the slip effect. In this section, the simulated porosity is set as 0.1 for shale patch, and TOC is equal to 0.12. Meanwhile, the maximum pore diameters of organic and inorganic matter are given as 200 and 2 nm. Besides, the minimum pore diameters of organic and inorganic matter are given as 30 and 1 nm. Moreover, the contact angles of organic and inorganic matter are set as 150 and 30°, and the bulk viscosity of the confined fluid can be calculated by eq 4 when the system temperature is 300 K.

$$K_{al} = GA^{-(1+D_T)/2}\left\{\frac{\lambda_{max}^{3+D_T}}{3+D_T-D_f}\left[1-\left(\frac{\lambda_{min}}{\lambda_{max}}\right)\right]^{3+D_T-D_f} + \frac{L_{st}\lambda_{max}^{2+D_T}}{2+D_T-D_f}\left[1-\left(\frac{\lambda_{min}}{\lambda_{max}}\right)\right]^{2+D_T-D_f}\right\} \quad (31)$$

Here, absolute error (eq 32) represents the deviation between the certain value of analytical permeability obtained from eq 31 and FMC permeability; meanwhile, the relative error (eq 33) is the ratio of absolute errors to the certain value of analytical permeability obtained from eq 31.

$$\delta_a = K_{ef} - K_{al} \quad (32)$$

$$\delta_r = \frac{\delta_a}{K_{ef}} = \frac{K_{ef}-K_{al}}{K_{ef}} \quad (33)$$

where δ_a and δ_r are the absolute error and relative error for the FMC simulation. K_{ef} is FMC permeability and K_{al} is analytical permeability obtained from eq 31.

Figure 3 shows the results of FMC with 3000 runs, and it can be found that FMC permeability oscillated with a certain

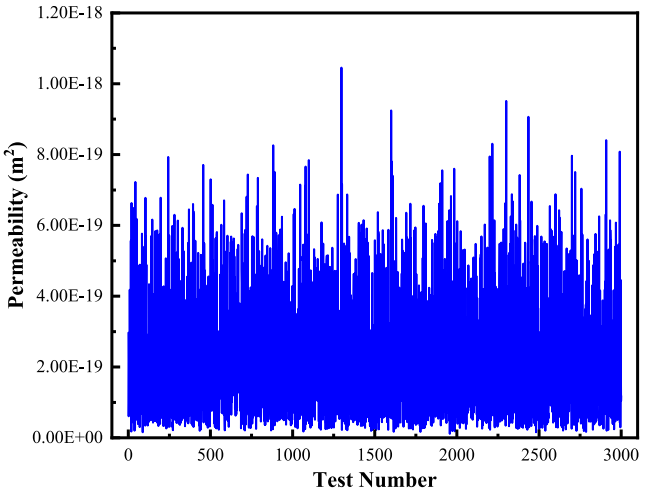

Figure 3. Permeability of MC simulation for every run.

number. The certain value of analytical permeability for this case is equal to 2.13×10^{-19} m^2. As shown in Figure 4 (blue line), the average summation is made, and it can be found that average FMC permeability approaches a stable value of 2.27×10^{-19} m^2 with the increase of the test number. In addition, absolute and relative errors are only 0.14×10^{-19} m^2 and 6.51%, respectively, which illustrate the correctness of FMC. Another phenomenon is that when the test number exceeds 1000 times, the relative error of FMC is less than 10% (orange line), which is important to guide the applications of FMC.

4. RESULTS AND DISCUSSION

In this section, the impact of different transport mechanisms, shale wettability, and pore characteristic parameters on the water flow in shale matter is investigated. In order to remove the uncertainty of the Monte Carlo (MC) simulation, average

https://doi.org/10.1021/acsomega.3c07609
ACS Omega 2023, 8, 48280−48291

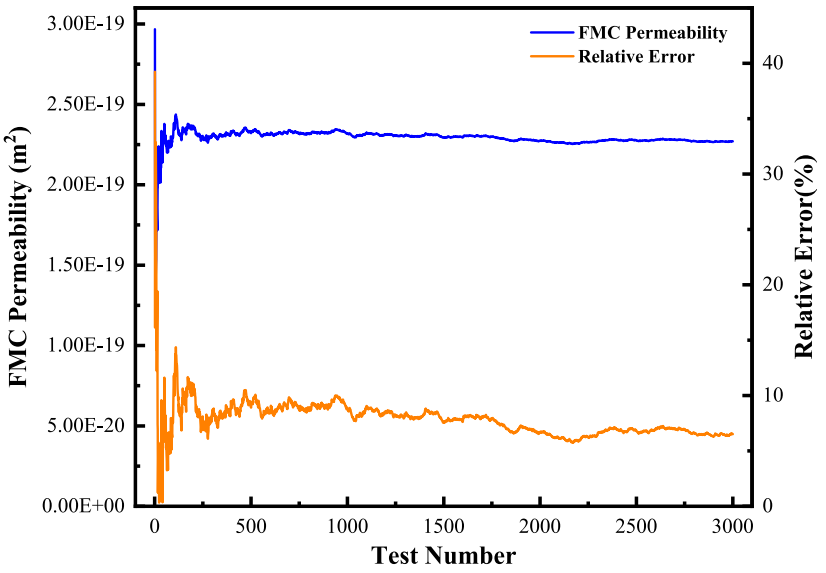

Figure 4. Results of average FMC permeability and relative error.

Table 2. Basic Parameters for the Simulations

parameters	value	unit	description
φ	0.1		shale porosity[34,35]
$\lambda_{om,max}$	20/30/40	nm	maximum pore diameter of organic matter[34]
$\lambda_{in,max}$	100/200/300	nm	maximum pore diameter of inorganic matter[34]
$\lambda_{om,min}$	0.5/1/1.5	nm	minimum pore diameter of organic matter[34]
$\lambda_{in,min}$	1/2/3	nm	minimum pore diameter of inorganic matter[34]
TOC	0.12		organic matter content[35]
θ_{om}	130/150/170	°	contact angle of organic matter[34]
θ_{in}	20/30/40	°	contact angle of inorganic matter[34]
T	300	K	system temperature[35]

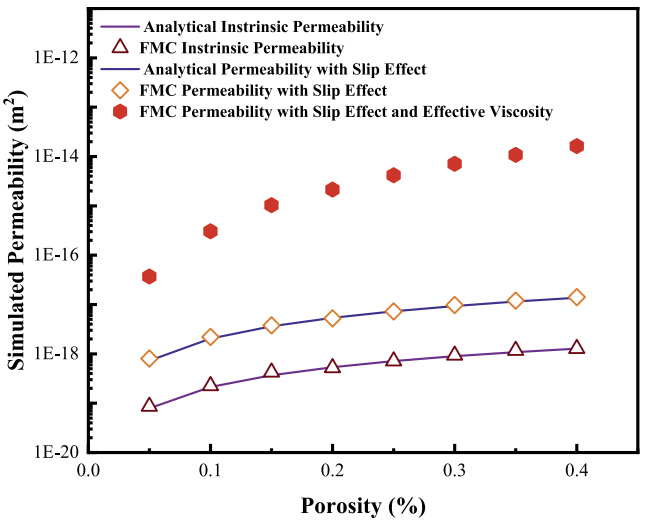

Figure 5. Influence of transport mechanisms for liquid flow in organic matter.

values are calculated for all results of FMC simulations. The basic parameters for the simulations are given in Table 2.

4.1. Influence of Transport Mechanisms. Figures 5 and 6 illustrate the influence of transport mechanisms for organic

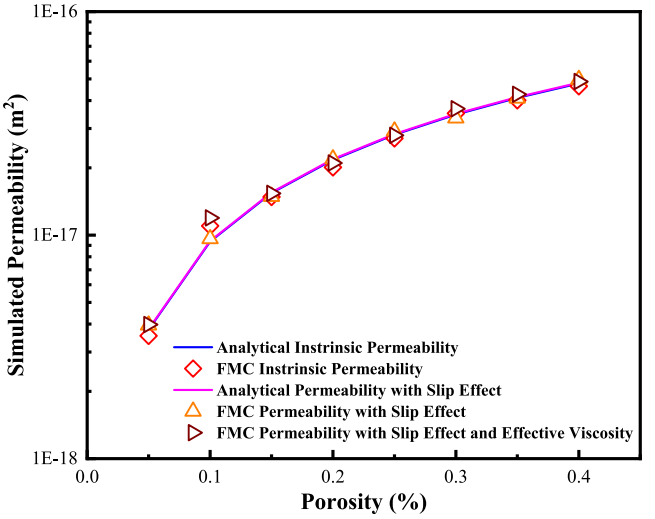

Figure 6. Influence of transport mechanisms for liquid flow in inorganic matter.

and inorganic matter. It is proven again that FMC permeabilities (orange triangle and yellow diamond) match well with analytical solutions for intrinsic and slip-corrected permeabilities (green and blue lines) in both organic and inorganic matter. Then, FMC permeabilities considering the slip effect and effective viscosity are 2−3 orders of magnitude larger than intrinsic and slip-corrected permeabilities in organic matter, as shown in Figure 5.

However, special transport mechanisms including the slip effect and effective viscosity have little influence on water flow in inorganic matter, as shown in Figure 6. Two reasons for this case are that hydrophilic inorganic surface results in the multilayer sticking effect,[21] which reduces the water flow capacity in inorganic matter. With the increase of pore size, the viscous force dominates the liquid flow, which weakens the influence of the slip effect. Hence, a much large fracturing fluid loss usually happens at an organic-rich shale system.

4.2. Influence of Shale Wettability. Shale wettability plays an important role in liquid transport in nanoscale porous media because of the relationship among slip effect, effective

https://doi.org/10.1021/acsomega.3c07609
ACS Omega 2023, 8, 48280−48291

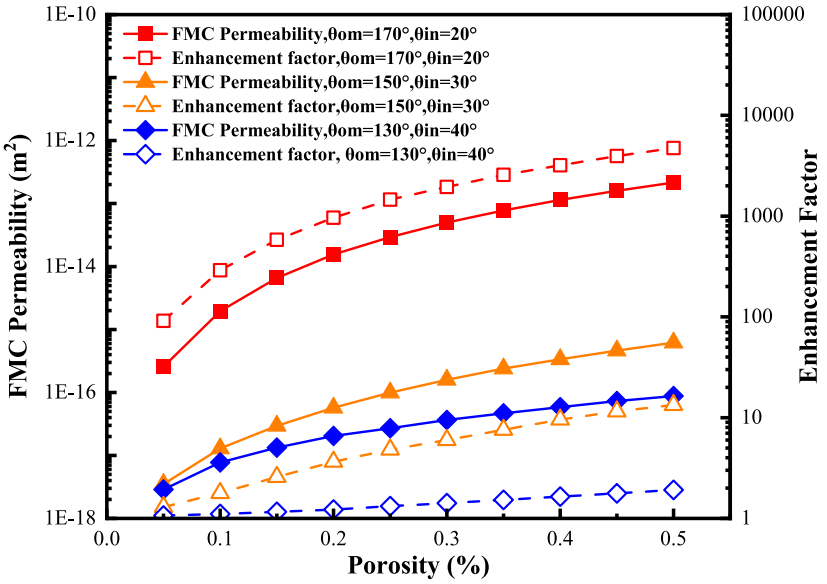

Figure 7. Influence of shale wettability with different microscopical contact angles.

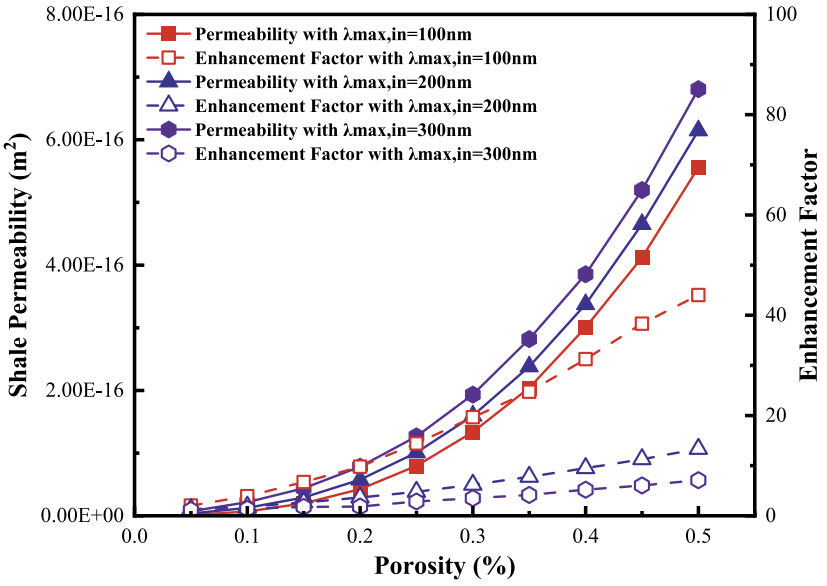

Figure 8. Influence of maximum inorganic pore diameters for permeability and enhancement factor.

liquid viscosity, and contact angle. Inorganic matter usually includes quartz, calcite, feldspar, and clay, which reflect the hydrophilic pore surface ($0°<\theta_{in}<90°$). Organic matter also consists of various hydrophobic organic kerogen ($90°<\theta_{om}<180°$). Hence, shale matrix usually exhibits a dual-wettability feature in macroscopic perspective, and contact angles from the Duvernay basin shale range from 65 to 103°, which are usually detected by polished shale rock experiments.[14] Cassie and Baxter[59] proposed the quantitative relationship between the macroscopic contact angle and two-component microscale contact angles, as shown in eq 34.

$$\cos(\theta_{eff}) = \omega\cos(\theta_{om}) = (1-\omega)\cos(\theta_{in}) \quad (34)$$

where θ_{eff} is the effective macroscopic contact angle, °; ω is the fraction of organic pore surface area.

Figure 7 presents the effect of shale wettability with different inorganic and organic contact angles. It can be noted that the close macroscopic wettability ($\theta_{eff}=80°$) for three research cases exists although organic and inorganic matter contain different microscopic wettabilities (different contact angles). However, the simulated effective permeability of liquid transport produces a quite large difference. It can be found that with θ_{om} increasing and θ_{in} decreasing, the effective permeability of the whole shale matrix grows in number. On the other hand, the enhancement factor in the situation of $\theta_{om}=170°$ and $\theta_{in}=20°$ is 4 orders of magnitude larger than the case of $\theta_{om}=130°$ and $\theta_{in}=40°$, and this phenomenon illustrates that the water flow capacity will enhance with the increase of microscopical hydrophobicity for organic and inorganic systems, which means that a much large fracturing fluid loss can be more prone to happen in the microscopical hydrophilic shale system.

4.3. Influence of Pore Geometric Parameters.

According to the established FMC model in Section 2, both fractal parameters and pore geometric parameters affect the effective shale permeability. Meanwhile, a series of theoretical

https://doi.org/10.1021/acsomega.3c07609
ACS Omega 2023, 8, 48280−48291

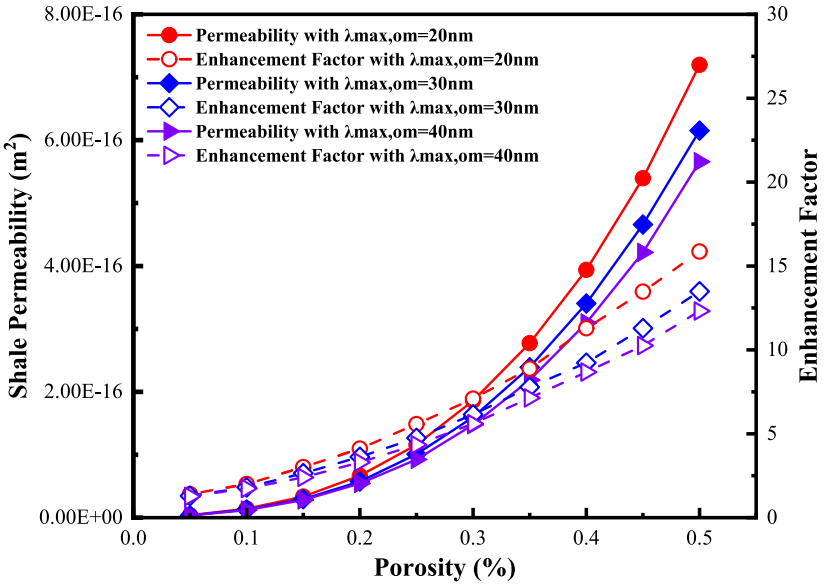

Figure 9. Influence of maximum organic pore diameters for permeability and enhancement factor.

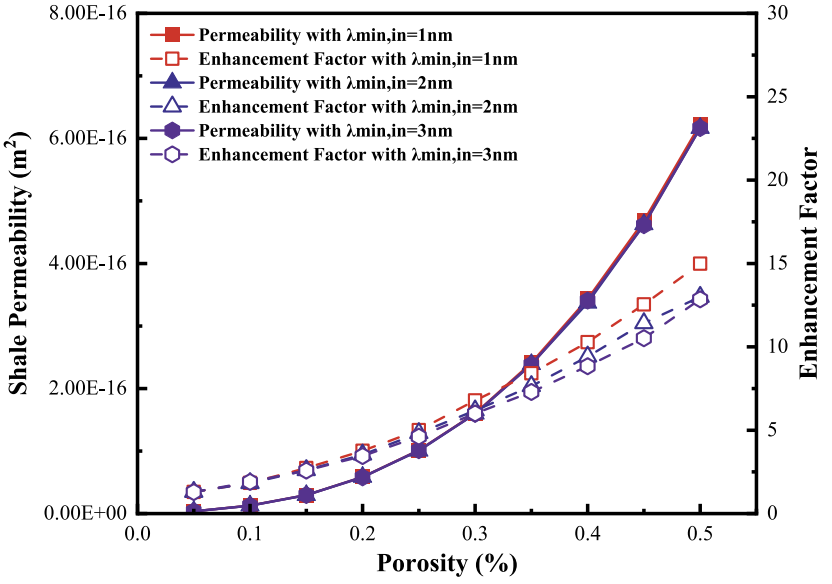

Figure 10. Influence of minimum inorganic pore diameters for permeability and enhancement factor.

methods have been put forward to bridge the relationship between fractal parameters (D_f, D_t) and pore geometric parameters (φ, λ_{max}, λ_{min}), as shown in Eqs 14−17. Hence, only pore geometric parameters are investigated for the organic and inorganic matter, respectively, in this work.

Figures 8−11 show the effects of pore geometric parameters on the shale permeability and enhancement factor. First of all, all simulated results illustrate that shale permeability increases rapidly with the increase of porosity because more interconnected pores contribute to shale permeability. Figures 8 and 10 present the influence of maximum pore diameters for organic and inorganic matter on the shale permeability and enhancement factor. Results show that shale permeabilities grow in number with the increase of maximum pore diameters. However, enhancement factor has the opposite trend, which means that the intention of slip effect can weaken up for the large pores. Figures 10 and 11 show the influence of minimum pore diameters for organic and inorganic matter on the shale permeability and enhancement factor. Although minimum inorganic pore diameters vary from 1 to 3 nm, both shale permeability and enhancement factor only have a tiny change. However, minimum organic pore diameters have significant impacts on liquid flow in the shale system, as shown in Figure 11. Besides, the shale permeability inclines, with the minimum organic pore diameters decreasing from 1.5 to 0.5 nm, and the enhancement factor also rapidly increases with the same trend of shale permeability. Thus, it can be concluded that with the minimum organic pore diameters declining in our cases, the interaction between water and pore walls becomes more stronger, which results in the strong near-wall slip effect and larger shale permeability. Another remarkable phenomenon that should be noted is that the enhancement factor is close to 1 when minimum organic pore diameter is equal to 1.5 nm, which means that the slip effect can be ignored for organic pores, and the viscous force dominates liquid flow in this situation.

https://doi.org/10.1021/acsomega.3c07609
ACS Omega 2023, 8, 48280−48291

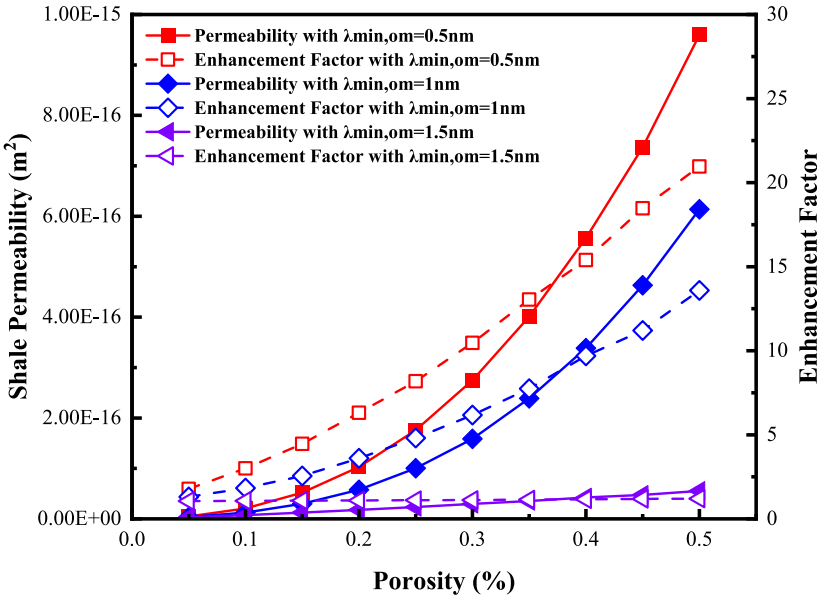

Figure 11. Influence of minimum organic pore diameters for permeability and enhancement factor.

5. CONCLUSIONS

In this paper, we focus on the confined liquid transport in a dual-wettability shale system. Specific conclusions of this research are summarized as follows:

(1) With the test number increasing, average FMC permeability approaches a stable analytical solution. FMC permeability matches well with the analytical solutions for intrinsic and slip-corrected permeabilities in both organic and inorganic matter.

(2) FMC permeabilities considering the slip effect and effective viscosity are 2−3 orders of magnitude larger than the intrinsic and slip-corrected permeabilities in organic matter. However, slip effect and effective viscosity have little influence on water flow in inorganic matter.

(3) With θ_{om} increasing and θ_{in} decreasing, the effective permeability of whole shale matrix grows in number. The enhancement factor in the situation of θ_{om} = 170° and θ_{in} = 20° is 4 orders of magnitude larger than the case of θ_{om} = 130° and θ_{in} = 40°, and this phenomenon illustrates that the variance of shale microscopic wettability has the important impact on the confined fluid transport.

(4) Shale permeability grows in number with the increase of maximum pore diameters, but enhancement factor has the opposite trend. The variance of minimum inorganic pore diameters has a tiny impact on liquid flow. However, minimum organic pore diameters have the significant impacts on liquid flow in shale system, and the enhancement factor also rapidly increases with the same trend of shale permeability.

AUTHOR INFORMATION

Corresponding Authors

Tuo Liang − *Xi'an Shiyou University, Xi'an 710065, China*; orcid.org/0009-0005-4511-5332; Email: ta.liang@foxmail.com

Changhua Yang − *Xi'an Shiyou University, Xi'an 710065, China*; Email: ych569@126.com

Ming Qu − *Sanya Offshore Oil and Gas Research Institute, Northeast Petroleum University, Sanya 572025, China*; Email: m.qu@foxmail.com

Authors

Weipeng Fan − *CNOOC Research Institute, Beijing 100028, China; China University of Petroleum (East China), Qingdao 266580, China*

Bo Yu − *Technology Monitoring Center of PetroChina Changqing Oilfield Company, Xi'an 710018, China*

Complete contact information is available at: https://pubs.acs.org/10.1021/acsomega.3c07609

Notes

The authors declare no competing financial interest.

ACKNOWLEDGMENTS

This work has been sponsored by Shaanxi Province Postdoctoral Research Project (2023BSHTBZZ45). Financial supports from the CNPC Innovation Found (grant no. 2021DQ02-0202) and National Natural Science Foundation of China (grant no. 52174046) are also significantly acknowledged.

REFERENCES

(1) Aguilera, R. Flow units: From conventional to tight-gas to shale-gas to tight-oil to shale-oil reservoirs. *SPE Reservoir Eval. Eng.* **2014**, *17*, 190−208.

(2) Jarvie, D.; Hill, R.; Ruble, T.; Pollastro, R. M. Unconventional shale-gas systems: The Mississippian Barnett Shale of north-central Texas as one model for thermogenic shale-gas assessment. *AAPG bulletin.* **2007**, *91*, 475−499.

(3) Yuan, J.; Luo, D.; Feng, L. A review of the technical and economic evaluation techniques for shale gas development. *Appl. Energy* **2015**, *148*, 49−65.

(4) Solarin, S.; Gil-Alana, L.; Lafuente, C. An investigation of long range reliance on shale oil and shale gas production in the US market. *Energy* **2020**, *195*, 116933.

(5) Hughes, J. A reality check on the shale revolution. *Nature* **2013**, *494* (7437), 307−308.

(6) Middleton, R.; Gupta, R.; Hyman, J.; Viswanathan, H. S. The shale gas revolution: Barriers, sustainability, and emerging opportunities. *Appl. Energy* **2017**, *199*, 88−95.
(7) Wang, Q.; Chen, X.; Jha, A.; Rogers, H. Natural gas from shale formation-the evolution, evidences and challenges of shale gas revolution in United States. *Renewable Sustainable Energy Rev.* **2014**, *30*, 1−28.
(8) Engelder, T.; Cathles, L.; Bryndzia, L. The fate of residual treatment water in gas shale. *J. Unconv. Oil Gas Resour.* **2014**, *7*, 33−48.
(9) Pagels, M.; Hinkel, J.; Willberg, D.; Moving beyond the capillary suction time test. *SPE International Symposium and Exhibition on Formation Damage Control*; OnePetro, 2012.
(10) Zhou, Q.; Dilmore, R.; Kleit, A.; Wang, J. Y. Evaluating fracture-fluid flowback in Marcellus using data-mining technologies. *SPE Prod. Oper.* **2016**, *31* (02), 133−146.
(11) Ghanbari, E.; Dehghanpour, H. The fate of fracturing water: A field and simulation study. *Fuel* **2016**, *163*, 282−294.
(12) Xu, S.; Gou, Q.; Hao, F.; Zhang, B.; Shu, Z.; Lu, Y.; Wang, Y. Shale pore structure characteristics of the high and low productivity wells, Jiaoshiba shale gas field, Sichuan Basin, China: Dominated by lithofacies or preservation condition. *Mar. Pet. Geol.* **2020**, *114*, 104211.
(13) Javadpour, F.; Singh, H.; Rabbani, A.; Babaei, M.; Enayati, S. Gas flow models of shale: a review. *Energy Fuels* **2021**, *35* (4), 2999−3010.
(14) Yassin, M.; Begum, M.; Dehghanpour, H. Organic shale wettability and its relationship to other petrophysical properties: A Duvernay case study. *Int. J. Coal Geol.* **2017**, *169*, 74−91.
(15) Kuila, U.; Prasad, M. Specific surface area and pore-size distribution in clays and shales. *Geophys. Prospect.* **2013**, *61*, 341−362.
(16) Hu, Y.; Devegowda, D.; Striolo, A.; Van Phan, A. T.; Ho, T. A.; Civan, F.; Sigal, R. Microscopic dynamics of water and hydrocarbon in shale-kerogen pores of potentially mixed wettability. *SPE J.* **2015**, *20* (01), 112−124.
(17) Zhan, S.; Su, Y.; Jin, Z.; Wang, W.; Cai, M.; Li, L.; Hao, Y. Molecular insight into the boundary conditions of water flow in clay nanopores. *J. Mol. Liq.* **2020**, *311*, 113292.
(18) Zhao, J.; Kang, Q.; Yao, J.; Zhang, L.; Li, Z.; Yang, Y.; Sun, H. Lattice Boltzmann simulation of liquid flow in nanoporous media. *Int. J. Heat Mass Transfer* **2018**, *125*, 1131−1143.
(19) Wang, W.; Wang, H.; Su, Y.; Tang, M.; Xu, J.; Zhang, Q. Simulation of liquid flow transport in nanoscale porous media using lattice Boltzmann method. *J. Taiwan Inst. Chem. Eng.* **2021**, *121*, 128−138.
(20) Afsharpoor, A.; Javadpour, F. Liquid slip flow in a network of shale noncircular nanopores. *Fuel* **2016**, *180*, 580−590.
(21) Wu, K.; Chen, Z.; Li, J.; Li, X.; Xu, J.; Dong, X. Wettability effect on nanoconfined water flow. *Proc. Natl. Acad. Sci. U.S.A.* **2017**, *114* (13), 3358−3363.
(22) Sun, Z.; Wu, K.; Shi, J.; Zhang, T.; Feng, D.; Huang, L.; Li, X. An analytical model for transport capacity of water confined in nanopores. *Int. J. Heat Mass Transfer* **2019**, *138*, 620−630.
(23) Lan, Q.; Xu, M.; Binazadeh, M.; Dehghanpour, H.; Wood, J. M. A comparative investigation of shale wettability: The significance of pore connectivity. *J. Nat. Gas Sci. Eng.* **2015**, *27* (2), 1174−1188.
(24) Arif, M.; Zhang, Y.; Iglauer, S. Shale Wettability: Data Sets, Challenges, and Outlook. *Energy Fuels* **2021**, *35* (4), 2965−2980.
(25) Zhao, G.; Yao, Y.; Adenutsi, C. D.; Feng, X.; Wang, L.; Wu, W. Transport Behavior of Oil in Mixed Wettability Shale Nanopores. *ACS Omega* **2020**, *5* (49), 31831−31844.
(26) Yu, B.; Li, J. Some fractal characters of porous media. *Fractals* **2001**, *09* (03), 365−372.
(27) Yu, B.; Cheng, P. A fractal permeability model for bi-dispersed porous media. *Int. J. Heat Mass Transfer* **2002**, *45* (14), 2983−2993.
(28) Cai, J.; Yu, B. Prediction of maximum pore size of porous media based on fractal geometry. *Fractals* **2010**, *18* (04), 417−423.
(29) Cai, J.; Luo, L.; Ye, R.; Zeng, X.; Hu, X. Recent advances on fractal modeling of permeability for fibrous porous media. *Fractals* **2015**, *23* (01), 1540006.
(30) Li, C.; Lin, M.; Ji, L.; Jiang, W.; Cao, G. Investigation of intermingled fractal model for organic-rich shale. *Energy Fuels* **2017**, *31* (9), 8896−8909.
(31) Yang, F.; Ning, Z.; Liu, H. Fractal characteristics of shales from a shale gas reservoir in the Sichuan Basin, China. *Fuel* **2014**, *115*, 378−384.
(32) Li, A.; Ding, W.; He, J.; Dai, P.; Yin, S.; Xie, F. Investigation of pore structure and fractal characteristics of organic-rich shale reservoirs: A case study of Lower Cambrian Qiongzhusi formation in Malong block of eastern Yunnan Province, South China. *Mar. Pet. Geol.* **2016**, *70*, 46−57.
(33) Wang, Q.; Cheng, Z. A fractal model of water transport in shale reservoirs. *Chem. Eng. Sci.* **2019**, *198*, 62−73.
(34) Zhang, T.; Li, X.; Shi, J.; Sun, Z.; Yin, Y.; Wu, K.; Li, J.; Feng, D. An apparent liquid permeability model of dual-wettability nanoporous media: A case study of shale. *Chem. Eng. Sci.* **2018**, *187*, 280−291.
(35) Naraghi, M.; Javadpour, F. A stochastic permeability model for the shale-gas systems. *Int. J. Coal Geol.* **2015**, *140*, 111−124.
(36) Zeng, F.; Zhang, Y.; Guo, J.; Ren, W.; Jiang, Q.; Xiang, J. Prediction of shale apparent liquid permeability based on fractal theory. *Energy Fuels* **2020**, *34* (6), 6822−6833.
(37) Yu, B.; Zou, M.; Feng, Y. Permeability of fractal porous media by Monte Carlo simulations. *Int. J. Heat Mass Transfer* **2005**, *48* (13), 2787−2794.
(38) Yang, J.; Wang, M.; Wu, L.; Liu, Y.; Qiu, S.; Xu, P. A novel Monte Carlo simulation on gas flow in fractal shale reservoir. *Energy* **2021**, *236*, 121513.
(39) Xiao, B.; Chen, H.; Xiao, S.; Cai, J. Research on relative permeability of nanofibers with capillary pressure effect by means of Fractal-Monte Carlo technique. *J. Nanosci. Nanotechnol.* **2017**, *17* (9), 6811−6817.
(40) Su, H.; Zhang, Y.; Xiao, B.; Huang, X.; Yu, B. A fractal-monte carlo approach to model oil and water two-phase seepage in low-permeability reservoirs with rough surfaces. *Fractals* **2021**, *29* (01), 2150003.
(41) Xu, P.; Qiu, S.; Yu, B.; Jiang, Z. Prediction of relative permeability in unsaturated porous media with a fractal approach. *Int. J. Heat Mass Transfer* **2013**, *64*, 829−837.
(42) Chen, A.; Miao, T.; Li, Z.; et al. Fractal Monte Carlo simulations of the effective permeability for a fractured network. *Fractals* **2022**, *30*, 2250074.
(43) Xu, P.; Yu, B.; Qiao, X.; Qiu, S.; Jiang, Z. Radial permeability of fractured porous media by Monte Carlo simulations. *Int. J. Heat Mass Transfer* **2013**, *57* (1), 369−374.
(44) Xiao, B.; Wang, S.; Wang, Y.; Jiang, G.; Zhang, Y.; Chen, H.; Liang, M.; Long, G.; Chen, X. Effective thermal conductivity of porous media with roughened surfaces by fractal-monte carlo simulations. *Fractals* **2020**, *28* (02), 2050029.
(45) Rojas-Altamirano, G.; Vargas, R.; Escandón, J. P.; Mil-Martínez, R.; Rojas-Montero, A. Calculation of Effective Thermal Conductivity for Human Skin Using the Fractal Monte Carlo Method. *Micromachines* **2022**, *13* (3), 424.
(46) Xu, Y.; Zheng, Y.; Kou, J. Prediction of effective thermal conductivity of porous media with fractal-monte Carlo simulations. *Fractals* **2014**, *22* (03), 1440004.
(47) Javadpour, F.; McClure, M.; Naraghi, M. Slip-corrected liquid permeability and its effect on hydraulic fracturing and fluid loss in shale. *Fuel* **2015**, *160*, 549−559.
(48) Zhang, T.; Javadpour, F.; Yin, Y.; Li, X. Upscaling water flow in composite nanoporous shale matrix using lattice Boltzmann method. *Water Resour. Res.* **2020**, *56* (4), No. e2019WR026007.
(49) Fan, D.; Ettehadtavakkol, A.; Wang, W. Apparent liquid permeability in mixed-wet shale permeable media. *Transp. Porous Media* **2020**, *134* (3), 651−677.

https://doi.org/10.1021/acsomega.3c07609
ACS Omega 2023, 8, 48280−48291

(50) Laliberte, M. Model for calculating the viscosity of aqueous solutions. *J. Chem. Eng. Data* **2007**, *52* (2), 321−335.
(51) Kalra, A.; Garde, S.; Hummer, G. Osmotic water transport through carbon nanotube membranes. *Proc. Natl. Acad. Sci. U.S.A.* **2003**, *100* (18), 10175−10180.
(52) Thomas, J.; McGaughey, A. Density, distribution, and orientation of water molecules inside and outside carbon nanotubes. *J. Chem. Phys.* **2008**, *128* (8), 084715.
(53) Yu, B. Analysis of flow in fractal porous media. *Appl. Mech. Rev.* **2008**, *61* (5), 050801.
(54) Yu, B.; Liu, W. Fractal analysis of permeabilities for porous media. *AIChE J.* **2004**, *50* (1), 46−57.
(55) Wu, T.; Li, X.; Zhao, J.; Zhang, D. Multiscale pore structure and its effect on gas transport in organic-rich shale. *Water Resour. Res.* **2017**, *53* (7), 5438−5450.
(56) Romero-Sarmiento, M. F.; Ducros, M.; Carpentier, B.; Lorant, F.; Cacas, M. C.; Pegaz-Fiornet, S.; Wolf, S.; Rohais, S.; Moretti, I. Quantitative evaluation of TOC, organic porosity and gas retention distribution in a gas shale play using petroleum system modeling: Application to the Mississippian Barnett Shale. *Mar. Pet. Geol.* **2013**, *45*, 315−330.
(57) Li, J.; Chen, Z.; Wu, K.; Zhang, T.; Zhang, R.; Xu, J.; Li, R.; Qu, S.; Shi, J.; Li, X. Effect of water saturation on gas slippage in circular and angular pores. *AIChE J.* **2018**, *64* (9), 3529−3541.
(58) Gao, Q.; Han, S.; Cheng, Y.; Li, Y.; Yan, C.; Han, Z. Apparent permeability model for gas transport through micropores and microfractures in shale reservoirs. *Fuel* **2021**, *285*, 119086.
(59) Cassie, A.; Baxter, S. Wettability of porous surfaces. *Trans. Faraday Soc.* **1944**, *40*, 546−551.

https://doi.org/10.1021/acsomega.3c07609
ACS Omega 2023, 8, 48280−48291